We are IntechOpen,
the world's leading publisher of
Open Access books
Built by scientists, for scientists

6,900
Open access books available

186,000
International authors and editors

200M
Downloads

Our authors are among the

154
Countries delivered to

TOP 1%
most cited scientists

12.2%
Contributors from top 500 universities

CLARIVATE ANALYTICS
BOOK
CITATION
INDEX
INDEXED

WEB OF SCIENCE™

Selection of our books indexed in the Book Citation Index
in Web of Science™ Core Collection (BKCI)

Interested in publishing with us?
Contact book.department@intechopen.com

Numbers displayed above are based on latest data collected.
For more information visit www.intechopen.com

Multilayered Wire Media: Generalized Additional Boundary Conditions and Applications

Alexander B. Yakovlev, Yashwanth R. Padooru,
George W. Hanson and Chandra S.R. Kaipa

Additional information is available at the end of the chapter

http://dx.doi.org/10.5772/36937

1. Introduction

The history of homogenization methods describing the interaction of electromagnetic waves with materials/matter (formed by a large number of periodic metal-lattices/atoms) goes a long way back (see, for a detailed historical review, the books by [1] and [2]). Typically, these methods are applied when the size of the material inclusions is small compared to the wavelength of the incident wave. In such cases, the microscopic fluctuations are averaged out to obtain smooth and slowly varying macroscopic quantities that can be used to characterize the long range variations of the electromagnetic waves [3].

In recent years, there has been an increased interest in homogenization methods characterizing artificial materials (such as metamaterial structures). In particular, materials that constitute wire media have attracted special attention, due to their ability in enabling interesting phenomena such as negative refraction [4, 12] and sub-wavelength imaging [6, 7], among others. It has been recently shown in [8] that wire media exhibits strong spatial dispersion at microwaves, and that the constitutive relations between the macroscopic fields and the electric dipole moment are non-local [5]. Due to the non-local character of the material, solving the reflection and transmission problems at interfaces associated with wire media becomes difficult. This is because the non-local character of the material enables it to support extra (or extraordinary) waves, which in general are not supported by materials with local responses. To overcome this, uniquely solved ABCs [9–11, 13] which are pertinent to the specific problem (composition of the structure) can be introduced.

In [10], the scattering problem of a wire-medium slab (consisting of long parallel array of thin-metallic wires normal to the interface) was solved by deriving an ABC at the interface of the wire medium and a dielectric material. Here the ABC was derived based on the fact that the microscopic current must vanish at the tip of the wires and that the

macroscopic fields must satisfy the ABC at the interface. The above result was extended to study the reflection characteristics of a textured surface [9], wherein the metallic wires are connected to a ground plane. In this scenario, the ABC was derived by taking into account that the microscopic electric charge density vanishes at the connection of wire end to the ground plane. Later, the ABC developed in [9] was applied to characterize the reflection and transmission properties of the single-layer [14, 15] and multilayer mushroom-type structures [17] (composed of metallic patches). It should be noted that these structures (single-layer and multilayer) were shown to suppress spatial dispersion in wire media. This is because the presence of metallic patches at the wire ends diminishes charge buildup in such a way that, upon homogenization, the mushroom structure can be treated as a uniaxial continuous Epsilon-Negative (ENG) material loaded with a capacitive grid of patches. Further, in [13] generalized additional boundary conditions (GABCs) have been derived for wire media terminated with distributed loads (metallic patch arrays acting as parallel loads to the wires) and lumped loads (arbitrary impedance insertions acting as series loads to the wires) or a combination of both at the junction, with the latter case presented in [18, 19]. Although, the GABCs derived in [13] are applied at the wire-to-patch connection with the finite size of the patch (with certain restrictions imposed on the size of the gap between the patches with respect to the separation of adjacent patch arrays), these boundary conditions are valid only for perfect electric conductor terminations. However, when the metallic terminations (patches) are thin (resistive) (or for no patch case [10]), the charge accumulation and diffusion at the wire-to-patch interface (or charge accumulation at the open wire end interface) becomes important (spatial dispersion effects have to be considered), necessitating a new additional boundary condition at this interface [16], which takes into account the finite conductivity of the material at the connection points. Upon homogenization, these charge effects are reflected in the nonlocal slab permittivity. The ABC developed in the later case (thin patch) is a generalized form from which one can easily obtain the ABCs derived in [9] and [10].

The ABC derived in [16] can only be applied to a single-layer wire-medium slab terminated with either PEC or thin resistive (metal/graphene) patches or a combination of both. It is derived under the hypothesis that the material adjacent to it is either free space or a dielectric filled material. However, for a more general configuration shown in Fig. 1 (where the metallic wires of one wire-medium slab are connected to another wire medium with a thin resistive patch at the junction), the ABC proposed in [16] cannot be applied.

In our recent paper [26] we further extend the theory of [16] and study the reflection properties of a more general case of a multilayer mushroom-type structure composed of thin resistive patches with a typical configuration shown in Fig. 1. Based on charge conservation, new ABCs are derived at the interface of two uniaxial wire mediums with thin imperfect conductors at the junction. The scattering problem is solved by imposing the classical boundary conditions (at the thin resistive patch interface and at the ground plane), and the new additional boundary conditions obtained at the wire-to-patch junctions. To illustrate the application of the homogenization model with the new ABCs, we characterize the reflection properties of the multilayer structure, demonstrating that such a configuration with proper choice of the geometrical parameters acts as an absorber. Interestingly, it is noticed that the presence of vias results in the enhancement of the absorption bandwidth and an improvement in the absorptivity performance for increasing angles of the obliquely incident TM-polarized plane wave. The results obtained using the homogenization model for the proposed structure are validated against full-wave numerical simulations.
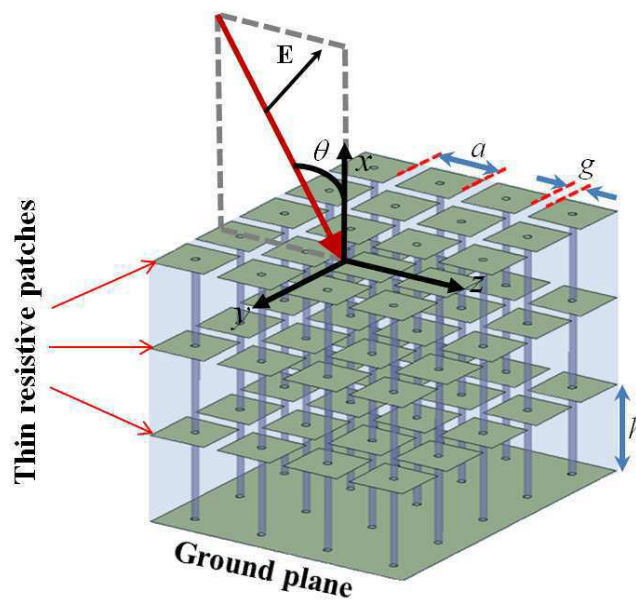
Figure 1. Geometry of a multilayer mushroom structure formed by periodically loading a grounded wire medium with thin resistive patches.

The chapter is organized as follows. In Section 2, at first, a review of the ABCs for the wire media is provided. Then, generalized ABCs at the wire-to-thin-resistive-patch junction are derived and the formalism of the nonlocal homogenization model is presented for the analysis of the reflection characteristics of the multilayer mushroom-type structure. The results of the single-layer, two-layer, and three-layer mushroom structures composed of thin resistive patches are discussed in Section 3. Finally, concluding remarks are given in Section 4.

2. Homogenization of multilayered mushroom-type HIS structures

In this section, at first a brief review of the recently derived ABCs [9, 10, 16] for wire media with applications to mushroom structures [14–17] is given (see Section 2.1). It should be noted that the configurations studied in [14–16] are single-layer mushroom structures (wire media loaded with patch arrays) with/without ground planes, and the one studied in [17] was a multilayer mushroom structure without a ground plane. In all these cases, except the one studied in [16], the vias, the patches, and the ground plane have all been assumed to be perfect electric conductors (PECs). In [16], the vias, and the ground plane are assumed to be PECs, however, the patch is a thin 2-D material. In [26] we study a multilayer structure (shown in Fig. 1) that is backed by a perfect electrically conducting ground plane, and assume that the vertical wires are PEC conductors and that the patches are arbitrary thin resistive materials. Secondly, we show the derivation of ABCs for the interface of two uniaxial wire mediums with thin imperfect conductors at the junction (see Section 2.2). Finally, the reflection problem of the multilayer structure (shown in Fig. 1) will be solved for the obliquely incident TM-polarized plane waves (see Section 2.3).

Referring to [8], it is known that the wire-medium slab is strongly spatially dispersive, and supports three different modes: transverse electric (TE^x), transverse magnetic (TM^x), and transverse electromagnetic (TEM) modes. Since TE incident waves do not interact with the wires, the study is restricted to only TM incident waves. In what follows, the term *microscopic*

refs to currents and fields in the microstructure of the medium, i.e., on the wires and patches of the actual physical structure. The term *macroscopic* refers to fields averaged over the lattice period, i.e., the fields in the equivalent homogenized (continuous) medium. In the following, a time variation of the form $e^{j\omega t}$ is assumed and suppressed.

2.1. Additional boundary conditions for wire media

The wire medium consists of an array of long metallic parallel wires arranged in a periodic lattice as shown in Fig. 2. The wires are oriented along the x-direction and are embedded in a host medium with permittivity ε_r. Solving the scattering problem for the wire-medium slab (which supports three modes) with the regular classical boundary conditions is impossible. To overcome this, an ABC is necessary. The ABC is derived by identifying some property of the wire-medium slab which gives a relation between the macroscopic fields, which in turn provides an extra degree of freedom to solve the scattering problem.
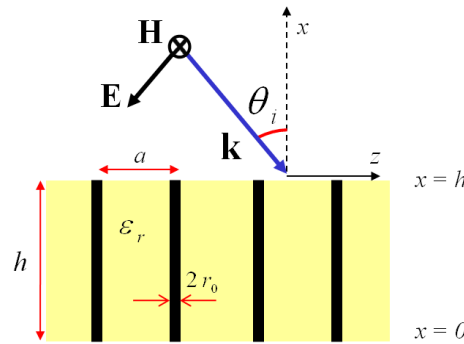

Figure 2. Geometry of a wire-medium slab with thickness h illuminated by a TM- polarized plane wave.

In [10], the authors showed that when the wire medium is adjacent to a nonconductive medium (such as air) and that the wires are thin, the microscopic current must vanish at the wire end $x = x_0$,

$$J_c(x_0) = 0 \tag{1}$$

and that the macroscopic field must satisfy the ABC at the interface with air [11],

$$\varepsilon_r \mathbf{E} \cdot \hat{x}|_{\text{wire medium side}} = \mathbf{E} \cdot \hat{x}|_{\text{air side}} \tag{2}$$

or, equivalently, the macroscopic field condition

$$k_0 \varepsilon_r E_x(x_0) - k_z \eta_0 H_y(x_0) = 0 \,. \tag{3}$$

However, the ABC (3) is not valid when the wire medium is adjacent to a conducting material, such as a perfect electrically conducting ground plane (shown in Fig. 3). In such a scenario, the microscopic current (J_c) at the wire-to-patch interface does not vanish and thus the ABC (3) is no longer applicable. The authors in [9, 10] have shown that it is relatively simple to derive the boundary condition for the wire-to-PEC interface. More specifically, they proved that the electric density of surface charge, σ_c, in a wire must vanish at the connection with the PEC ground plane,
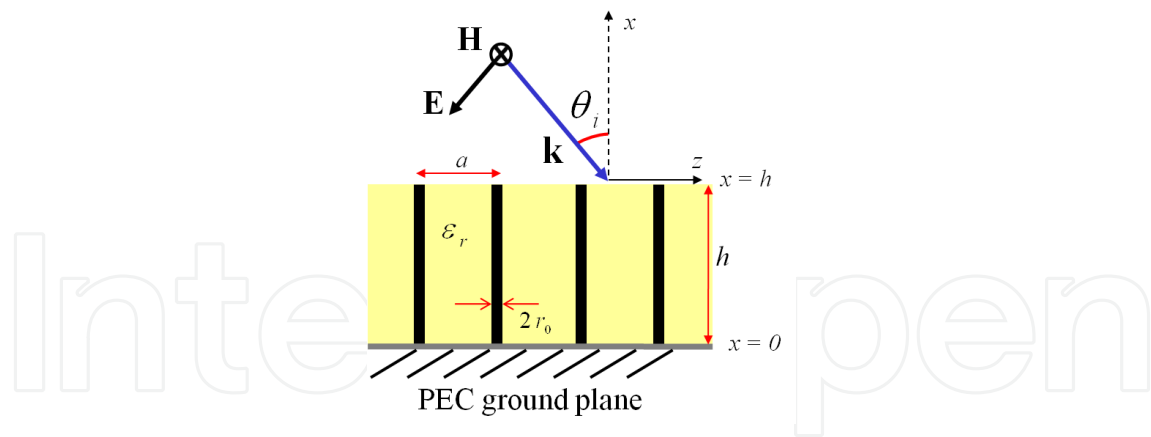
Figure 3. Geometry of a wire-medium slab connected to a ground plane.

$$\sigma_c = 0 \,(\text{at the interface}) \tag{4}$$

which necessitates that

$$\frac{\mathrm{d}J_c(x)}{\mathrm{d}x}\bigg|_{x=0^+} = 0 \tag{5}$$

or, in terms of macroscopic fields,

$$\left(k_0\varepsilon_r \frac{\mathrm{d}E_x(x)}{\mathrm{d}x} - k_z\eta_0 \frac{\mathrm{d}H_y(x)}{\mathrm{d}x}\right)\bigg|_{x=0^+} = 0 \,. \tag{6}$$

The above derived ABC (6) has been successfully applied by many researchers to various configurations of interest in which wire media were connected to one or many conducting elements (2-D array of patches). The most important of these configurations is the so-called mushroom structure [21] (wire media loaded with PEC pacthes and backed by a ground plane) which can be used in the design of high-impedance surfaces [14, 15] (shown in Fig. 4(a)) and metamaterials with negative refraction [17] (shown in Fig. 4(b)), among others.
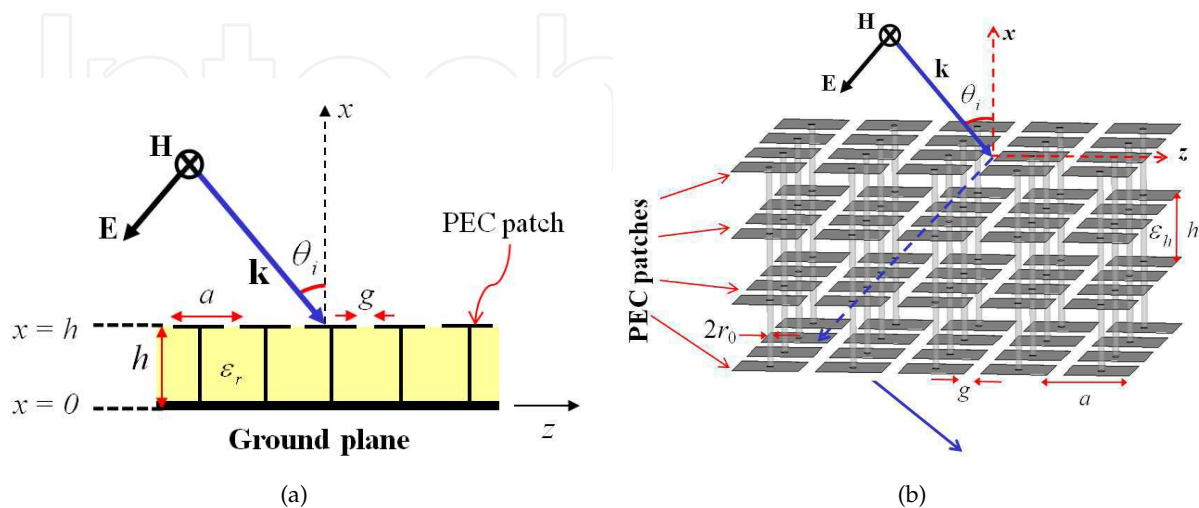

(a)   (b)

Figure 4. Mushroom-type wire medium structure: (a) Single-layer structure. (b) Multilayered structure.

However, this ABC applies only to a wire-to-PEC interface. When the skin depth is such that the field penetrates throughout the material, the PEC model is a very poor approximation of the actual physics. In this case, we need an ABC for a wire connected to an imperfect conductor, or, more generally, to an arbitrary material characterized by its complex conductivity. The same problem occurs when trying to model the ground plane or patch as a 2-D material, such as graphene or a 2-D electron gas. To answer this, the authors in [16] derived a generalized ABC for the wire-thin-metal-patch interface. The ABC is derived based on the principle of conservation of charge and that the microscopic wire current must satisfy the boundary condition,

$$\left(J_c(x) + \frac{\sigma_{2D}}{j\omega\varepsilon_0\varepsilon_r} \frac{\mathrm{d}J_c(x)}{\mathrm{d}x} \right) |_{x=h^-} = 0 \tag{7}$$

or, in terms of macroscopic field condition,

$$\left(1 + \frac{\sigma_{2D}}{j\omega\varepsilon_0} \frac{\mathrm{d}}{\mathrm{d}x} \right) \left[k_0 E_x(x) - \frac{k_z\eta_0}{\varepsilon_r} H_y(x) \right] |_{x=h^-} = 0. \tag{8}$$

In the limiting case of $\sigma_{2D} \to 0$, we have the wire medium (bed-of-nails) result (3), and for $\sigma_{2D} \to \infty$, we have the PEC patch result (6). Hence, (7) is the generalized form of ABC for the wire-thin-metal-patch interface (or for any conductivity of the thin-resistive patch).

The ABC (7) is valid as long as the material adjacent to it is nonconductive (such as air). If there is another spatially dispersive material (such as wire media) adjacent to it (see Fig. 1), then the ABC given by (7) is no longer valid. In the next subsection we derive a generalized ABC for the two uniaxial wire media with a thin resistive patch at the junction [26]. However, when two wire mediums are connected with a PEC patch at the junction (see Fig. 4(b), for the multilayer structure with PEC patches), GABCs similar to those proposed in [13] (for the PEC patches) have to be considered at the connection $x = x_0$:

$$\frac{\mathrm{d}J_c(x)}{\mathrm{d}x}\bigg|_{x_0^+} + \frac{\mathrm{d}J_c(x)}{\mathrm{d}x}\bigg|_{x_0^-} = \frac{2C}{C_0} \left[J_c(x_0^+) - J_c(x_0^-) \right] \tag{9}$$

$$\frac{\mathrm{d}J_c(x)}{\mathrm{d}x}\bigg|_{x_0^+} - \frac{\mathrm{d}J_c(x)}{\mathrm{d}x}\bigg|_{x_0^-} = 0 \tag{10}$$

where C is the capacitance of the wires and C_0 is the capacitance of the metallic patch which depends on the period a and gap g (the values of C and C_0 are defined in [13]). These ABCs are accurate for moderate and large gaps between the patches, provided the distance h between the metallic patches in adjacent layers is much greater than g. When the gap between the patches reduces and $C_0 \to \infty$, we have a perfect electric conducting ground plane with the ABCs (9), (10) reduced to $\mathrm{d}J_c(x)/\mathrm{d}x|_{x_0^+} = \mathrm{d}J_c(x)/\mathrm{d}x|_{x_0^-} = 0$, which is the same expression obtained above from (5). The PEC-ABC (5) is applicable at the junction of wire-PEC-wire interface, because the electric surface charge density on the wires will vanish independently at the junction making the fields in one media independent of the other. However, for the

case of thin-resistive patch at the junction, this is not the case, where charge diffusion and accumulation takes place with the fields in one wire media interacting with the ones in the other. Hence an ABC is necessary for this kind of interface (wire-thin-resistive-patch-wire).

2.2. Additional boundary condition for the junction of uniaxial wire media with thin resistive patch at the interface

Consider a plane wave incident on the configuration shown in Fig. 5, which consists of two uniaxial wire mediums with a thin resistive sheet (or in general, an arbitrary 2-D material such as graphene or a 2-D plasma characterized by a complex surface conductivity) placed at the interface $x = x_0$. Let a be the lattice period, σ_{2D} be the complex *surface* conductivity of the thin resistive patch (such as graphene patches with the surface conductivity given in [22]), r_1 and r_2 be the wire radii with $r_{1,2} \ll a$, and $\varepsilon_{r,1}$ and $\varepsilon_{r,2}$ be the corresponding dielectric host material for the two uniaxial wire media. For thin materials with *bulk* conductivity σ_{3D}, the surface conductivity can be written as $\sigma_{2D} = \sigma_{3D}t = 1/R_s$, where $t \ll \delta$ is the material thickness, $\delta = \sqrt{2/\omega\mu_0\sigma_{3D}}$ is the skin depth, and R_s is the sheet resistance. To understand how a thin resistive material (with bulk conductivity) is made see [29]. The resistive sheets can also be realized using commercially available resistive materials.

Due to the presence of discontinuities at the junction (sheet and different properties of the wire media, i.e., different wire radii and host permittivities) one can expect irregularities in the charge and the current distributions close to the junction. Let $J_{w,1}$ and $J_{w,2}$ be the microscopic current densities on the surface of the wires in mediums 1 and 2, and ρ_{s1} and ρ_{s2} be the surface charge densities on the PEC wires with radii r_1 and r_2, respectively, which are given by $\rho_{s1}(x) = \varepsilon_0\varepsilon_{r,1}E_{n1}(x)$ and $\rho_{s2}(x) = \varepsilon_0\varepsilon_{r,2}E_{n2}(x)$, where E_{n1} and E_{n2} are the normal components of the microscopic electric fields at the wire surfaces. On the thin conductive sheet, assumed local and isotropic, the microscopic current and the field are related as $J_s(y,z) = \sigma_{2D}E_t$, where J_s is the surface current density and E_t is the tangential electric field on the sheet. It should be noted that the tangential fields on the sheet in mediums 1 and 2 are assumed to be continuous at $x = x_0$, i.e.,

$$E_{t1}(x_0^-) = E_{t2}(x_0^+) = E_t \ . \tag{11}$$

Considering that, at the wire-to-sheet and sheet-to-wire connection points (x_0^+ and x_0^-) the electric fields normal to the wires are the same as the tangential fields on the thin resistive sheet, we can write

$$E_{n1}(x_0^-) = E_{t1}(x_0^-) = \rho_{s1}(x_0^-)/(\varepsilon_0\varepsilon_{r,1}) \tag{12}$$
$$E_{n2}(x_0^+) = E_{t2}(x_0^+) = \rho_{s2}(x_0^+)/(\varepsilon_0\varepsilon_{r,2}) \ . \tag{13}$$

From the continuity equation for the wires $\rho_{si} = -(1/j\omega)dJ_{w,i}(x)/dx$ ($i = 1, 2$) one can write the surface charge densities at the connection points (x_0^+ and x_0^-) as

$$\rho_{s1}(x_0^-) = -(1/j\omega)(dJ_{w,1}(x)/dx)|_{x_0^-} \tag{14}$$
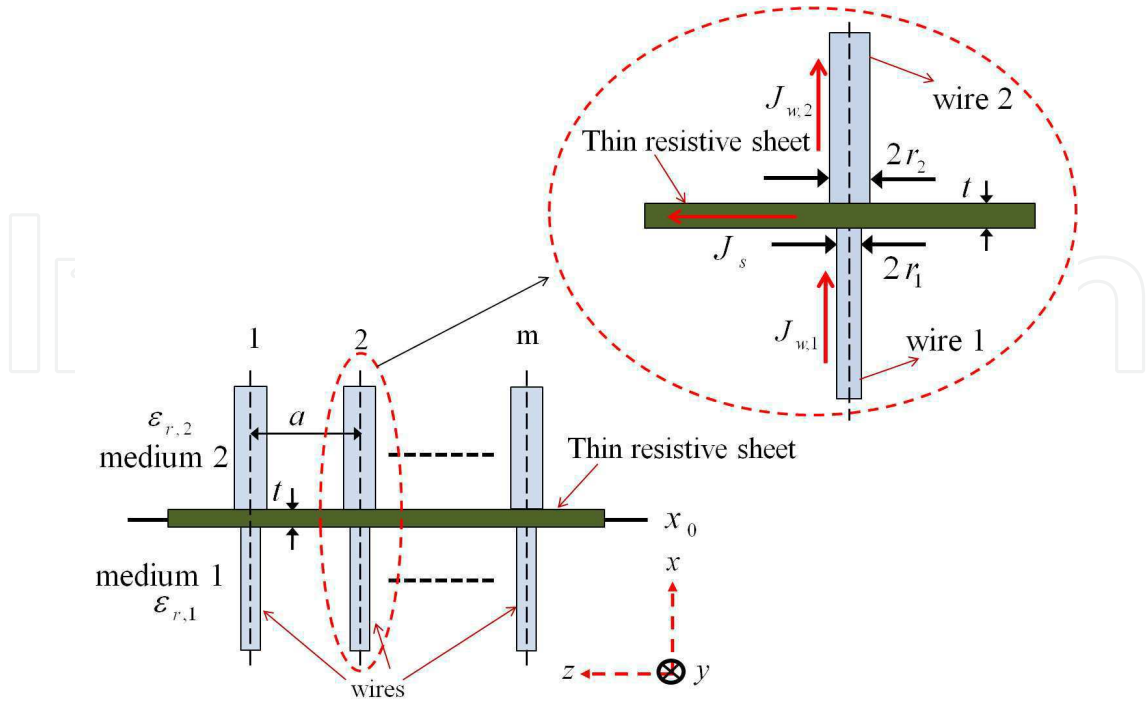$$\rho_{s2}(x_0^+) = -(1/j\omega)(dJ_{w,2}(x)/dx)|_{x_0^+} \ . \tag{15}$$

Figure 5. Geometry of a junction of two wire mediums with a thin resistive sheet at the interface.

Applying Kirchoff's current law (conservation of charge) at the junction of two wire mediums with thin resistive sheet at the interface (from Fig. 5), we have

$$J_s = J_{w,1} - J_{w,2} \, . \tag{16}$$

Using (11), the surface current density can be expressed as

$$\begin{aligned} J_s &= \sigma_{2D}E_t = \sigma_{2D}E_{t1}(x_0^-) = \sigma_{2D}E_{t2}(x_0^+) \\ &= \sigma_{2D}[E_{t1}(x_0^-) + E_{t2}(x_0^+)]/2 \, . \end{aligned} \tag{17}$$

Equating now (16) and (17), we have at the connection points

$$\sigma_{2D}[E_{t1}(x_0^-) + E_{t2}(x_0^+)]/2 = [J_{w,1}(x_0^-) - J_{w,2}(x_0^+)] \, . \tag{18}$$

Substituting the tangential fields (12)-(13) in (18), we can write

$$\sigma_{2D}[\rho_{s1}(x_0^-)/(\varepsilon_0\varepsilon_{r,1}) + \rho_{s2}(x_0^+)/(\varepsilon_0\varepsilon_{r,2})]/2 = [J_{w,1}(x_0^-) - J_{w,2}(x_0^+)] \, . \tag{19}$$

Now, using the surface charge densities of the two wires (14)-(15), in (19) we obtain the ABC

$$\frac{\sigma_{2D}}{2j\omega\varepsilon_0} \left[\frac{1}{\varepsilon_{r,1}} \frac{\mathrm{d}J_{w,1}(x)}{\mathrm{d}x} \Big|_{x_0^-} + \frac{1}{\varepsilon_{r,2}} \frac{\mathrm{d}J_{w,2}(x)}{\mathrm{d}x} \Big|_{x_0^+} \right] + [J_{w,1}(x_0^-) - J_{w,2}(x_0^+)] = 0. \tag{20}$$

Using the fact that the tangential fields are continuous at the thin conductive sheet interface (11), we obtain the second ABC for the microscopic wire current,

$$\frac{1}{\varepsilon_{r,1}} \frac{\mathrm{d}J_{w,1}(x)}{\mathrm{d}x}\Big|_{x_0^-} - \frac{1}{\varepsilon_{r,2}} \frac{\mathrm{d}J_{w,2}(x)}{\mathrm{d}x}\Big|_{x_0^+} = 0 \,. \tag{21}$$

In the next section, it will be shown that the ABCs (20) and (21) along with the classical boundary conditions will completely characterize the reflection properties of the multilayer mushroom-type HIS structure (shown in Fig. 1). Also, it is worth noting that the conditions (20) and (21) derived in this section are rather general and applicable to the cases of different conductivities of the thin conductive sheet at the wire-medium junction. In the limiting case of $\sigma_{2D} \to 0$ (transparent sheet), we have a continuous wire-medium slab with simple continuity conditions for the current: $J_{w,1}(x_0^-) = J_{w,2}(x_0^+)$ and $\varepsilon_{r,1}^{-1}\mathrm{d}J_{w,1}(x)/\mathrm{d}x|_{x_0^-} = \varepsilon_{r,2}^{-1}\mathrm{d}J_{w,2}(x)/\mathrm{d}x|_{x_0^+}$. For $\sigma_{2D} \to \infty$, we have a PEC conductor with the ABC for the wire microscopic currents given by $\mathrm{d}J_{w,1}(x)/\mathrm{d}x|_{x_0^-} = \mathrm{d}J_{w,2}(x)/\mathrm{d}x|_{x_0^+} = 0$, i.e., the derivative of each of the wire currents is independently zero at the connection points. This is consistent with the result of the single-sided wire-medium junction with a PEC conductor [10].

For the limiting case of the same host material on either side of the thin resistive sheet interface at x_0 (i.e., $\varepsilon_{r,1} = \varepsilon_{r,2} = \varepsilon_r$), the ABCs (20) and (21) can also be obtained by enforcing the continuity of surface charge densities and using the Kirchoff's current law at the connection points x_0^+ and x_0^- (the junction of wire media with thin resistive sheet at the interface), i.e., $\rho_{s1}(x_0^-) = \rho_{s2}(x_0^+) = \rho_s = \varepsilon_0\varepsilon_r J_s/\sigma_{2D} = (\rho_{s1}(x_0^-) + \rho_{s2}(x_0^+))/2$ and $J_{w,1} = J_s + J_{w,2}$.

It is interesting to note that (20) and (21) yield two independent ABCs. At first sight, this may seem inconsistent with the result of [16], which considered a single ABC to model the interfaces of wire media with an imperfect conductor. However, the reason why we obtain an extra ABC is quite simple. Here we consider the junction of two different wire mediums; that is, we have a spatially dispersive material on both sides of the interface (a double-sided wire-medium junction). Quite differently, the configuration considered in [16] consists of a single-sided wire-medium junction because one of the semi-spaces separated by the interface is free space. To show this, consider the two ABCs (20) and (21). Rewritting them, we have

$$\left[\frac{1}{\varepsilon_{r,1}} \frac{\mathrm{d}J_{w,1}(x)}{\mathrm{d}x}\Big|_{x_0^-} + \frac{1}{\varepsilon_{r,2}} \frac{\mathrm{d}J_{w,2}(x)}{\mathrm{d}x}\Big|_{x_0^+}\right] = -\frac{2j\omega\varepsilon_0}{\sigma_{2D}}\left[J_{w,1}(x_0^-) - J_{w,2}(x_0^+)\right] = 0 \tag{22}$$

$$\frac{1}{\varepsilon_{r,1}} \frac{\mathrm{d}J_{w,1}(x)}{\mathrm{d}x}\Big|_{x_0^-} - \frac{1}{\varepsilon_{r,2}} \frac{\mathrm{d}J_{w,2}(x)}{\mathrm{d}x}\Big|_{x_0^+} = 0 \,. \tag{23}$$

By solving (22) and (23) and rearranging the terms, we can write

$$\frac{1}{\varepsilon_{r,1}} \frac{\mathrm{d}J_{w,1}(x)}{\mathrm{d}x}\Big|_{x_0^-} = -\frac{j\omega\varepsilon_0}{\sigma_{2D}}\left[J_{w,1}(x_0^-) - J_{w,2}(x_0^+)\right] \,. \tag{24}$$

Figure 6. Schematic of a generic multilayer mushroom structure formed by periodically loading grounded wire medium with thin resistive square patches (side view).

Assuming that there is no second wire medium, we have $J_{w,2} = 0$, then (24) can be expressed as

$$\frac{1}{\varepsilon_{r,1}} \frac{dJ_{w,1}(x)}{dx}\Big|_{x_0^-} = -\frac{j\omega\varepsilon_0}{\sigma_{2D}} J_{w,1}\left(x_0^-\right). \qquad (25)$$

or,

$$J_{w,1}(x_0^-) + \frac{\sigma_{2D}}{j\omega\varepsilon_0\varepsilon_{r,1}} \frac{dJ_{w,1}(x)}{dx}\Big|_{x_0^-} = 0 \qquad (26)$$

which corresponds exactly to the ABC derived in ([16], Eq. (5)). Therefore, while a single ABC is sufficient to describe the electrodynamics of a single-sided wire-medium junction, the general case of a double-sided junction requires two ABCs due to the increased number of degrees of freedom (i.e., extra waves can be generated on both sides of the junction). Hence, (20) and (21) are generalizations of the simpler case studied in [16].

2.3. Nonlocal homogenization of the multilayered mushroom-type HIS structure

In this section, we show how the ABCs (20) and (21) derived in the previous section are necessary to calculate the reflection properties of a multilayered mushroom-type HIS structure for a obliquely incident TM-polarized plane wave (with the geometry as that shown in Fig. 6). Each of the wires with via radii $r_l \ll a$ (where a is the period of the patches and vias) are embedded in a dielectric host media (which is homogeneous and isotropic) of thickness h_l, characterized by relative permittivity $\varepsilon_{r,l}$ and permeability of free space, and are loaded with 2-D periodic thin resistive patches of conductivity $\sigma_{2D,l}$ at the interfaces $d_l, l = 1, 2, \ldots, m$. Here, we assume that the wires are lossless (PEC).

The wire-medium slab is characterized by the nonlocal dielectric function [8, 9]

$$\varepsilon_{\text{eff},l} = \varepsilon_0\varepsilon_{r,l}[\varepsilon_{xx,l}(\omega, k_x)\hat{x}\hat{x} + \hat{y}\hat{y} + \hat{z}\hat{z}] \qquad (27)$$

where $\varepsilon_{xx,l}(\omega, k_x) = 1 - k_{p,l}^2/(k_{h,l}^2 - k_x^2)$, $k_{h,l} = k_0\sqrt{\varepsilon_{r,l}}$ is the wavenumber in the host material, k_0 is the wavenumber in free space, $k_{p,l}$ is the plasma wavenumber which depends on the period and radius of the vias: $k_{p,l}^2 = (2\pi/a^2)/[\ln(a/2\pi r_l) + 0.5275]$, and k_x is the x-component of the wave vector $\mathbf{k} = (k_x, 0, k_z)$. Let $J_{w,l}$ be the currents induced on the metallic wires. It is known that for a TM plane-wave incidence, the wire medium excites both TEM and TM^x modes, and thus, following [9], the magnetic field in all space is given by:

$$\eta_0 H_y = e^{\gamma_0(x-d_m)} + Re^{-\gamma_0(x-d_m)}, \text{ air side: } x > d_m \tag{28}$$

$$\eta_0 H_y^{(l)} = A_{\text{TM},l}^+ e^{\gamma_{\text{TM},l}(x-d_{l-1})} + A_{\text{TM},l}^- e^{-\gamma_{\text{TM},l}(x-d_{l-1})} + B_{\text{TEM},l}^+ e^{\gamma_{\text{TEM},l}(x-d_{l-1})}$$

$$+ B_{\text{TEM},l}^- e^{-\gamma_{\text{TEM},l}(x-d_{l-1})}, \text{ wire medium slab: } d_{l-1} < x < d_l \tag{29}$$

where $d_l = h_1 + h_2 + \ldots + h_l$, $l = 1, 2, \ldots, m$, $d_0 = 0$, $\eta_0 = \sqrt{\mu_0/\epsilon_0}$ is the free-space impedance, R is the reflection coefficient, $A_{\text{TM},l}^\pm$, $B_{\text{TEM},l}^\pm$ are the amplitude coefficients of the TM and TEM fields, $\gamma_0 = \sqrt{k_z^2 - k_0^2}$, $\varepsilon_{xx,l}^{\text{TM}} = 1 - k_{p,l}^2/(k_z^2 + k_{p,l}^2)$, $\gamma_{\text{TEM},l} = jk_0\sqrt{\epsilon_{r,l}}$, $\gamma_{\text{TM},l} = \sqrt{k_{p,l}^2 + k_z^2 - k_{h,l}^2}$, and $k_z = k_0 \sin\theta_i$. The corresponding electric fields can be expressed as follows:

$$E_z = \frac{-j\gamma_0}{k_0}\left[e^{\gamma_0(x-d_m)} - Re^{-\gamma_0(x-d_m)}\right], \text{ air side: } x > d_m \tag{30}$$

$$E_z^{(l)} = \frac{-j\gamma_{\text{TM},l}}{\varepsilon_{r,l}k_0}\left[A_{\text{TM},l}^+ e^{\gamma_{\text{TM},l}(x-d_{l-1})} - A_{\text{TM},l}^- e^{-\gamma_{\text{TM},l}(x-d_{l-1})}\right]$$

$$-\frac{j\gamma_{\text{TEM},l}}{\varepsilon_{r,l}k_0}\left[B_{\text{TEM},l}^+ e^{\gamma_{\text{TEM},l}(x-d_{l-1})} - B_{\text{TEM},l}^- e^{-\gamma_{\text{TEM},l}(x-d_{l-1})}\right],$$

$$\text{wire medium slab: } d_{l-1} < x < d_l \tag{31}$$

$$E_x^{(l)} = \frac{k_z}{\varepsilon_{xx,l}^{\text{TM}}k_0\varepsilon_{r,l}}\left[A_{\text{TM},l}^+ e^{\gamma_{\text{TM},l}(x-d_{l-1})} + A_{\text{TM},l}^- e^{-\gamma_{\text{TM},l}(x-d_{l-1})}\right],$$

$$\text{wire medium slab: } d_{l-1} < x < d_l. \tag{32}$$

To calculate the unknown coefficients, R, $A_{\text{TM},l}^\pm$, $B_{\text{TEM},l}^\pm$, we impose boundary conditions at $x = 0, d_1, d_2, \ldots, d_m$. Since, there are m dielectric layers and m interfaces, we have the total number of unknowns as $4m + 1$ (i.e., four unknowns in each layer corresponds to $4m$, and the remaining unknown is R). Hence, $4m + 1$ boundary conditions are necessary to calculate the $4m + 1$ unknown coefficients. At the thin resistive patch interfaces ($x = d_l^\pm$, $l = 1, \ldots, m$), the macroscopic two-sided impedance boundary conditions establish that the tangential electric ($E_z^{(l)}$) and magnetic fields ($H_y^{(l)}$), can be related via a sheet impedance, i.e.,

$$E_z^{(l)}\big|_{x=d_l^+} = E_z^{(l)}\big|_{x=d_l^-} = Z_{g,l}\left(H_y^{(l+1)}\big|_{x=d_l^+} - H_y^{(l)}\big|_{x=d_l^-}\right) \tag{33}$$

where $Z_{g,l}$ is the grid impedance of the thin conductive patches [16, 23, 24] given by

$$Z_{g,l} = \frac{a}{(a-g)\sigma_{2D,l}} - j\frac{\pi}{2\omega\varepsilon_0(\varepsilon_{r,l}^{qs})a\ln(\csc\frac{\pi g}{2a})} \tag{34}$$

where $\varepsilon_{r,l}^{qs} = (\varepsilon_{r,l} + \varepsilon_{r,l+1})/2$ for interior patches $(l = 1, 2, \ldots, m-1)$ and $\varepsilon_{r,m}^{qs} = (\varepsilon_{r,m} + 1)/2$ for the patch located at the upper interface $(l = m)$. This gives $2m$ boundary conditions. At the ground plane interface $(x = 0^+)$, we have two more boundary conditions [9]: i) tangential macroscopic total electric field vanishes $(E_z^{(1)}|_{x=0^+} = 0)$ and ii) derivative of current is zero $(dJ_{w,1}(x)/dx|_{x=0^+} = 0)$ or in terms of macroscopic fields [10]

$$\left[k_0\varepsilon_{r,1}\frac{dE_x^{(1)}(x)}{dx} - k_z\eta_0\frac{dH_y^{(1)}(x)}{dx}\right]|_{x=0^+} = 0. \tag{35}$$

Following [16], the boundary condition at the top patch interface, $x = d_m^-$, can be written as

$$J_{w,m}(d_m^-) + \frac{\sigma_{2D,m}}{j\omega\varepsilon_0\varepsilon_{r,m}}\frac{dJ_{w,m}(x)}{dx}|_{d_m^-} = 0 \tag{36}$$

or, equivalently, the macroscopic field condition

$$\left(1 + \frac{\sigma_{2D,m}}{j\omega\varepsilon_0}\frac{d}{dx}\right)\left[k_0E_x^m(x) - \frac{k_z\eta_0}{\varepsilon_{r,m}}H_y^m(x)\right]|_{d_m^-} = 0. \tag{37}$$

This gives the total number of $2m + 3$ conditions, clearly insufficient to calculate the $4m + 1$ unknown coefficients, which makes apparent the need of the ABCs derived in Section 2.2.

At the junction of two wire mediums with thin conductive patches at the interfaces $(x = d_l^{\pm}, l = 1, \ldots, m-1)$ it is necessary to impose the ABCs (20) and (21) (with the assumption that the gap between the patches is small), in addition to the boundary condition (33)

$$\frac{\sigma_{2D,l}}{2j\omega\varepsilon_0}\left[\frac{1}{\varepsilon_{r,l}}\frac{dJ_{w,l}(x)}{dx}|_{d_l^-} + \frac{1}{\varepsilon_{r,l+1}}\frac{dJ_{w,l+1}(x)}{dx}|_{d_l^+}\right]$$
$$+ [J_{w,l}(d_l^-) - J_{w,l+1}(d_l^+)] = 0 \tag{38}$$

$$\frac{1}{\varepsilon_{r,l}}\frac{dJ_{w,l}(x)}{dx}|_{d_l^-} - \frac{1}{\varepsilon_{r,l+1}}\frac{dJ_{w,l+1}(x)}{dx}|_{d_l^+} = 0. \tag{39}$$

In terms of macroscopic fields, (38) and (39) can be rewritten as

$$\left(1 + \frac{\sigma_{2D,l}}{2j\omega\varepsilon_0}\frac{d}{dx}\right)\left[k_0E_x^{(l)}(x) - \frac{k_z\eta_0}{\varepsilon_{r,l}}H_y^{(l)}(x)\right]|_{d_l^-} = \left(1 - \frac{\sigma_{2D,l}}{2j\omega\varepsilon_0}\frac{d}{dx}\right)\left[k_0E_x^{(l+1)}(x) - \frac{k_z\eta_0}{\varepsilon_{r,l+1}}H_y^{(l+1)}(x)\right]|_{d_l^+}$$

$$\tag{40}$$

$$\frac{\mathrm{d}}{\mathrm{d}x}\left[k_0 E_x^{(l)}(x) - \frac{k_z \eta_0}{\varepsilon_{r,l}} H_y^{(l)}(x)\right]\Big|_{d_l^-} = \frac{\mathrm{d}}{\mathrm{d}x}\left[k_0 E_x^{(l+1)}(x) - \frac{k_z \eta_0}{\varepsilon_{r,l+1}} H_y^{(l+1)}(x)\right]\Big|_{d_l^+}. \qquad (41)$$

Since there are $m-1$ layers of two-sided wire-medium junctions, we have $2(m-1)$ boundary conditions and hence, the total number of boundary conditions are equal to $4m+1$. Using the boundary conditions (33), (35), (8), (40), and (41), we can easily obtain a linear system for the $4m+1$ unknowns of the problem. This system can be solved either numerically or analytically for the unknown field coefficients, $A_{\mathrm{TM},l}^{\pm}$ and $B_{\mathrm{TEM},l}^{\pm}$, and the reflection coefficient R.

3. Numerical results

To illustrate the application of the proposed homogenization model, in this section we study the reflection properties of different multilayered mushroom-type HIS structures. To test the model, at first we analyze a single-layer wire medium loaded with an arbitrary material (a thin copper patch with finite bulk conductivity and a graphene patch characterized by its complex surface conductivity) at one end and a ground plane at the other. Next, we study the prospects of the multilayered mushroom-type HIS structure being used as an absorber. All the results obtained using the homogenization model are tested against the full-wave numerical simulations.

3.1. Single-layer mushroom structure with thin metal/graphene patches

As a first example, a single-layer mushroom-type HIS structure with geometry shown in Fig. 7 is chosen. In this configuration, the patches are copper and have a thickness of 60 nm. The parameters of the structure are: $a = 2$ mm, $g = 0.2$ mm, $h = 1$ mm, $r_0 = 0.05$ mm, and $\varepsilon_r = 10.2$. The analysis is performed for an obliquely incident TM-polarized plane wave. Fig. 8(a) shows the comparison of reflection magnitude behaviors calculated using HFSS and the proposed homogenization model for a TM-polarized plane wave incident at $30°$ to the normal. Also, in Fig. 8(a) we have included the result obtained using the wire-PEC ABC ([10], or (6)). Clearly, one can notice the difference between the results obtained using the ABC of the wire-PEC interface and the new ABC (GABC, wire-thin-metal interface - see (7) or (26)). In fact, the result obtained using the GABC is in good agreement with the HFSS [31] result.

Fig. 8(b) shows the behavior of reflection magnitude for a metal patch with $\sigma_{3\mathrm{D}}t = 0.058$ S (e.g. $t = 20$ nm and $\sigma_{3\mathrm{D}} = 2.9 \times 10^6$ S/m). The remaining parameters are the same as those considered in the previous example. Again, the results obtained using the new ABC (wire-thin-metal interface) are in good agreement with the HFSS results, whereas the results obtained using the old ABC (wire-PEC interface, (6)) deviate from the HFSS results.

Fig. 9 shows the reflection magnitude behavior for the mushroom structure loaded with graphene patches with a chemical potential of $\mu_c = 0.5185$ eV [see [22] for the surface conductivity of graphene] for a plane wave incident at $\theta = 45°$. For example, at $f = 11.96$ GHz the complex surface conductivity, $\sigma_{2\mathrm{D}} = 0.0304 - j0.0011$ S. Clearly, excellent agreement is seen between the GABC and the HFSS results. As is obvious, the ABC-PEC (6)
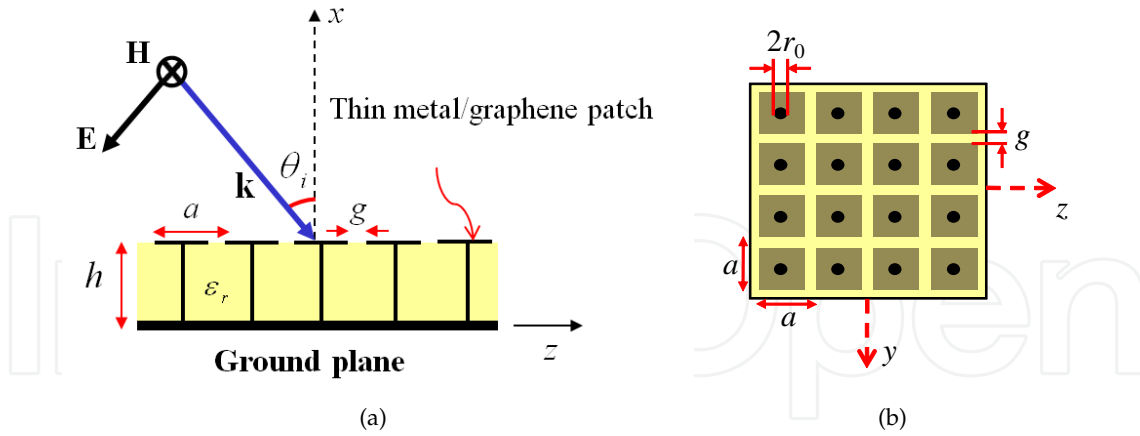
Figure 7. (a) Mushroom-type wire-medium structure with thin metal/graphene patches: (a) Side-view showing incident TM plane wave and (b) Top view of the structure.
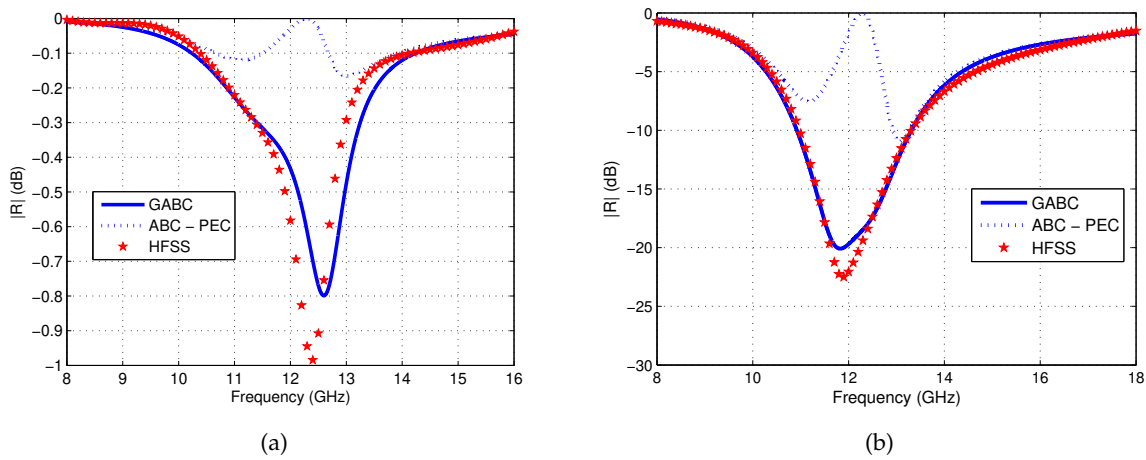

Figure 8. Reflection coefficient for a TM-polarized plane wave incident at $\theta = 30°$. (a) Copper patches with thickness 60 nm. (b) A material patch with $\sigma_{3D} t = 0.058$ S.

and local model [14] results give significant errors since this ABC assumes that the surface charge at the tip of the wires or at the wire-patch interface vanishes (4). This may hold true for the wire-PEC interface, but does not apply for the wire-thin-metal/graphene interface. This is because at the wire-thin-metal interface, charge accumulation and diffusion takes place and the fields completely penetrate the metal. Hence, a new ABC (GABC) is required to obtain the correct result.

Referring to Fig. 9, one can notice that the nonlocal model result (ABC-PEC) and the local model result agree well with each other. This is because, for the large chemical potential 0.5185 eV considered in this example, it seems that the spatial dispersion effects in the wire media are reduced, and the mushroom structure can be treated as a uniaxial continuous Epsilon-Negative material loaded with PEC patches (although this is not the case with the GABC, which sees the interface in a correct manner).
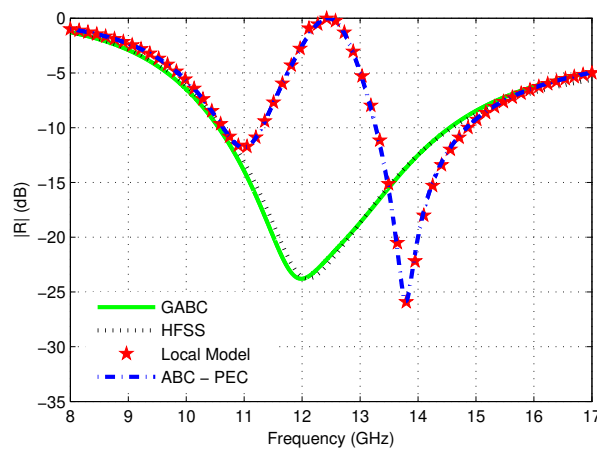
Figure 9. Reflection coefficient of the mushroom structure loaded with graphene patches with $\theta = 45°$.

Overall Figs. 8 and 9 show the effectiveness of the new ABC. Hence, when a PEC wire is connected to a thin-metal patch, as is the case considered here, the new ABC is the good choice to obtain the correct result.

To understand the behavior (effects of spatial dispersion) of the grounded wire-medium slab loaded with graphene patches, in Fig. 10 we plotted the normalized wire current along the vias for different values of bias (μ_c). It can be noticed that for zero bias ($\mu_c = 0$) the current is quite nonuniform and as the bias increases, the current becomes more and more uniform. This is because, for the case of zero bias the patch is almost transparent or in other words its conductivity (σ_{2D}) is very small (can be seen in Fig. 10) and behaves as a dielectric material rather than a metal. As the bias increases, the conductivity increases and the properties of the patch will be close to that of a metal (since, it is known that for a vias truncated with a PEC patch the current is uniform [14]). Hence, the current starts to become more and more uniform, indicating that the spatial dispersion effects are negligible and the wire-medium slab can be treated as a uniaxial continuous Epsilon Negative material [14, 15] loaded with patches. However, it should be noted that, despite the uniformity of the current for the case of $\mu_c = 0.5185$ eV, the homogenization model still needs an ABC to model the graphene patch mushroom structure, indicating that spatial dispersion effects are important for this structure. This is because, at the patch-to-wire interface, diffusion and accumulation of charge occurs (unlike at a wire-to-PEC interface, where surface charge vanishes) and an ABC is required to capture the physics.

By observing Figs. 8 and 9, one can notice a dip in the reflection magnitude curves for some values of the conductivity or the thickness of the metal patch. This behavior of showing reflection nulls allows the mushroom structures with thin-metal/graphene patches to be used in absorber applications. By properly selecting the parameters of the mushroom structure, one can easily obtain either a narrow band or even a wideband absorber. More on the design and analysis of realizing the absorbers is explored in the next section.

3.2. Design and analysis of multilayered mushroom-type HIS structures with applications to absorbers

In this section, we concentrate on the design and analysis of single-layer, two-layer, and three-layer mushroom structures for obliquely incident TM-polarized plane waves using the
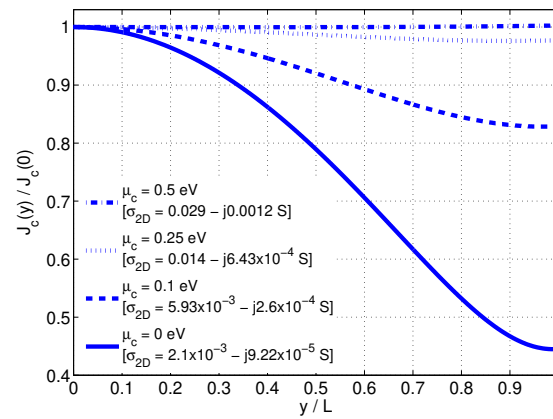
Figure 10. Normalized wire current for a graphene patch mushroom structure for different values of bias at $f = 14$ GHz.

proposed homogenization model. All the configurations are loaded with thin resistive sheets. The results obtained using the homogenization model are confirmed with the numerical HFSS simulations.

3.2.1. Single-layer mushroom HIS structure with thin resistive patches

Understanding the mechanism of the multilayered mushroom-type HIS structure as an absorber is quite a complicated task. Hence, to make it is easier to comprehend, we begin with the design and analysis of a simpler case, i.e., a single-layered mushroom HIS structure (with the geometry shown in Fig. 11). Although this structure is analyzed in the previous section, the aim here is to show that by proper selection of the mushroom structure parameters (such as periodicity, gap between the patches, height and permittivity of the dielectric substrate, radius of the vias, and resistivity of the patches) one can obtain remarkably attractive results (such as increase in the absorption bandwidth, enhancement in the absorption level, among others).
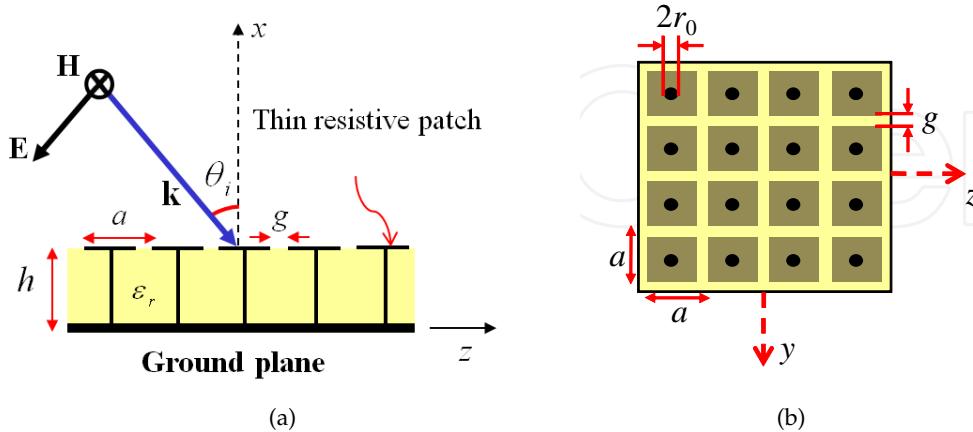
Figure 11. (a) Single-layer mushroom-type HIS absorber with thin resistive patches. (b) Top view of the structure.

To show this effect, we considered the following parameters in the design of the absorber: $a = 6.8$ mm, $g = 0.5$ mm, $h = 3.5$ mm, $r_0 = 0.08$ mm, $\varepsilon_r = 2.5$, and $R_s = 106.54\,\Omega$. The sheet resistance R_s, can be related to the grid impedance of the patch as follows: from (34) the grid

impedance of the lossy patch array can be represented as a series RC circuit $(R_g - j/(\omega C_g))$, where the real value corresponds to R_g (resistance per unit cell) given by $a/((a-g)\sigma_{2D})$ or $R_s a/(a-g)$ and C_g is the capacitance of the patch grid whose value can be obtained from (34). Although the selection of a particular value of R_s is a tedious process, the procedure will be discussed later in this section. In order to show the advantage of the mushroom-type absorber, we compare its reflection coefficient behavior against a similar structure but without vias. Figs. 12(a) and 12(b) show the reflection magnitude curves for
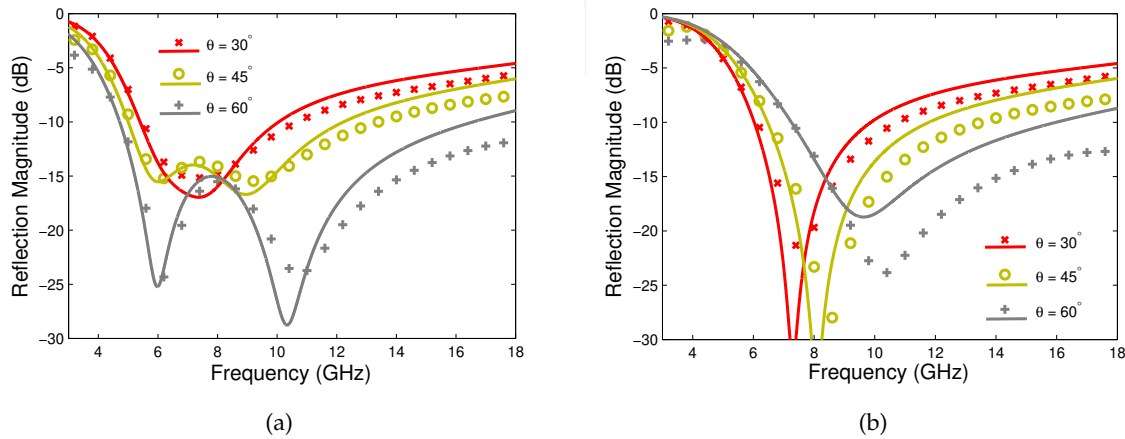
Figure 12. Comparison of analytical (solid lines) and full-wave HFSS results (crosses, circles, and plus signs) of the reflection coefficient for the single-layer HIS absorber excited by a TM-polarized plane wave at oblique angles of incidence θ: (a) with vias. (b) without vias.

$30°$, $45°$, and $60°$ for a TM-polarized plane wave. Referring to the results shown in Fig. 12(a), one can see good agreements between the analytical results and the full-wave HFSS results. The analytical results here are obtained using either the ABC given by (7) or (26) obtained in Section 2.2 as a limiting case for a single-sided wire-to-patch junction. However, the analytical results shown in Fig. 12(b) are obtained using the circuit theory model given in [20, 24, 25]. By comparing Figs. 12(a) and 12(b) one can see that for the structure with vias, the absorption bandwidth increases for increasing angles of incidence (i.e., the structure with vias gives a better performance than the structure without vias), although, one can notice a decrease in the absorption level for $30°$ and $45°$. Also, in Fig. 12(a) it is observed that the lower frequency bound of the absorption band (around 6 GHz) is stable, which is in complete contrast to the behavior of the structure without vias (Fig. 12(b)). This frequency stability can be attributed to the increased interaction of the incident wave with the vias [30].

To comprehend the nature of the mushroom structure and its reasons to act as a wideband absorber when compared to the structure without vias, we studied the reflection properties (phase and magnitude) of the mushroom structure for various sheet resistivities for a TM-polarized plane wave incident at $45°$ to the normal. Fig. 13 shows the reflection phase and magnitude for various resistive values of the patch ranging from 0 ($\sigma_{3D}t = \infty$, PEC case) to ∞ ($\sigma_{3D}t = 0$, transparent case) calculated using the nonlocal homogenization model discussed in Section 2.3. Starting with the PEC case, i.e., $R_s = 0$, the reflection phase behavior (shown in Fig. 13(a)) shows two resonances. One corresponding to $0°$ and the other corresponding to $360°$ (shown in red circles) acting as a HIS at the two frequencies. These resonances are such that one lies above the plasma frequency ($f_p/\sqrt{\varepsilon_r} = 6.28$ GHz) and the other lies below $f_p/\sqrt{\varepsilon_r}$, consistent with the result of the single-layer mushroom-type
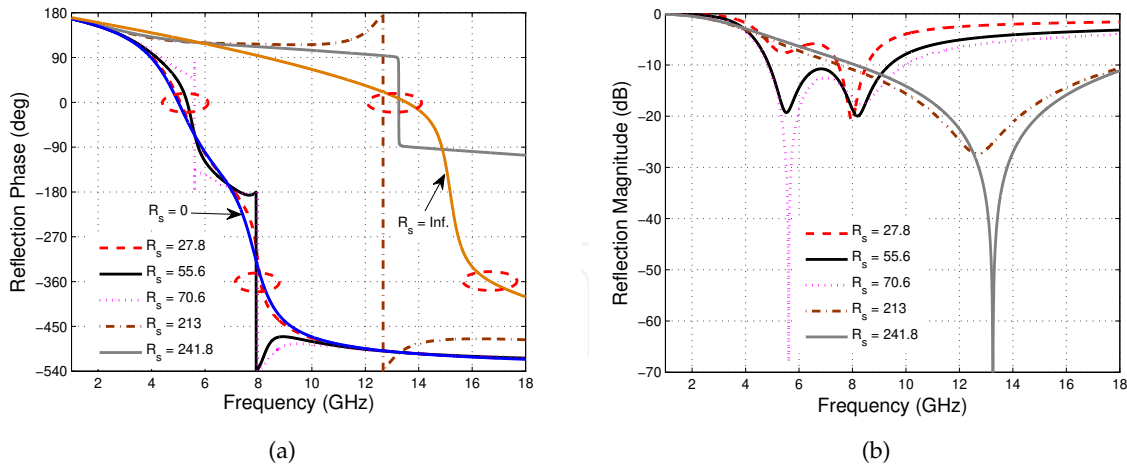
Figure 13. (a) Phase and (b) Magnitude of the reflection coefficient of the single-layer mushroom structure for different values of sheet resistivity R_s (in Ω), $\theta = 45°$.

HIS discussed in [14, 15] (although the dimensions and $f_p / \sqrt{\varepsilon_r}$ are different). With the increase in R_s, one can notice a deviation in the phase behavior from the actual HIS behavior. This deviation can be attributed to the change in the impedance of the mushroom structure due to change in the value of R_s. This deviation is referred to as perturbed HIS behavior. Corresponding to this in Fig. 13(b), the reflection magnitude curves show some deviations as R_s changes. The results in Fig. 13(b) can also be treated as the perturbed behavior of the HIS (the result of HIS when $R_s = 0$ is not included here, since its magnitude is unity).

At first glance, by noticing the results in Fig. 13(b) one might only comprehend that for different values of R_s there are different lossy patches, and hence, different reflection magnitudes. However, the results add meaning when they are seen with the increasing values of resistivities. Starting from $R_s = 27.8$ Ω, the reflection magnitude curve (dashed red curve) shows two partial nulls, which correspond closely to the two perturbed HIS resonances (shown in Fig.13(a)). With the further increase in the sheet resistivity, the two partial reflection nulls start to deviate in such a way that one of the null deepens and the other null either subdues or remains the same. As mentioned before, this is because as R_s changes, the grid impedance changes, which in turn changes the surface impedance of the mushroom structure. For example, for $R_s = 70.6$ Ω one of the reflection nulls has reached its minimum at 5.612 GHz (perfect match to free-space impedance) and the other reflection null is at the around 20 dB level, which is same as that of the second reflection null of $R_s = 27.8$ Ω case. Similarly, one can only see one deep reflection null for $R_s = 241.8$ Ω at 13.25 GHz. Based on these facts (how reflection nulls deviate), one can correlate the partial reflection magnitude curves (for the case of $R_s = 106.54$ Ω) in Fig. 12(a) with the perturbed HIS resonances. With the further increase in the sheet resistivity (for $R_s = \infty$, the patch array is fully transparent and we have a grounded wire-medium slab), the reflection phase behavior shown in Fig. 13(a) deviates further to the right and shows two resonances corresponding to $0°$ and $360°$ (acting as a HIS). Hence, for any value of R_s between 0 and ∞, the behavior of the structure should either resemble the properties of a perturbed HIS or a perturbed wire-medium slab. Thus, by utilizing the two resonances of the mushroom structure, and with the proper choice of the resistivity of the patch arrays one can increase the absorption bandwidth. This behavior of the mushroom structure which shows two resonances makes it

more attractive to consider compared to the structure without vias (which has only one HIS resonance, even when perturbed).
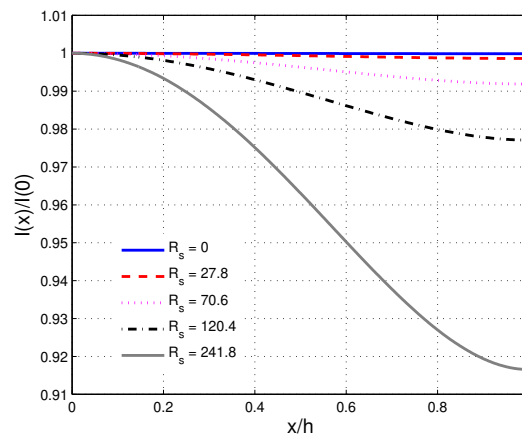

Figure 14. Normalized wire current in the single-layer mushroom structure for different values of sheet resistivity R_s (in Ω) at $f = 7\,\text{GHz}$, $\theta = 45^\circ$.

To further validate that the behavior observed in Fig. 12(a) is in fact due to the perturbed HIS behavior of the mushroom structure with PEC patches, we plotted the current behavior for various R_s varying from 0 to ∞. Fig. 14 shows the normalized wire current in the single-layer mushroom structure at $f = 7\,\text{GHz}$. It can be observed that for small values of resistivity ($R_s = 0$ to $120\,\Omega$), the current is uniform, which indicates that spatial dispersion effects are negligible (although requires the ABC (26)). This result is consistent with the result shown in Fig. 10, where the current distribution was uniform for large values of σ_{2D} indicating that spatial dispersion effects were almost negligible (although it required the ABC (26) to characterize the properties of the mushroom structure with graphene patches). Also, it should be noted that the value of R_s chosen in the design of absorber shown in Fig. 11 is in the range of 0 to $120.4\,\Omega$, hence the current behavior will be uniform similar to the case of mushroom structure with PEC patches, [14, 15]. Since, the current distribution is uniform and the phase behavior is close to that of the mushroom structure with PEC patches, the magnitude behavior or resonances of the absorber shown in Fig. 12(a) are indeed the perturbed HIS resonances of the mushroom structure with PEC patches.

Although the increase in absorption bandwidth and the enhancement in the absorption level is due to the presence of vias and proper choice of R_s, the absorption mechanism occurs mainly due to the lossy patch array. Since, the amount of energy lost or energy absorbed by the patch array is evaluated based on the value of R_s, it is important to determine the right value of R_s in designing wideband absorbers. The most common way is to use numerical optimization techniques such as [27, 28], among others. However, discussion of these techniques is beyond the scope of this work. Since, the analytical model gives the results instantaneously, it provides a reliable, fast, and efficient solution in selecting an optimum sheet resistance of the patch arrays. The idea is to obtain a certain range for R_s (in the range between the PEC case and wire-medium slab case) for each of the angles of incidence, where perfect reflection nulls are noticed for one of the two perturbed HIS resonances of the structure.
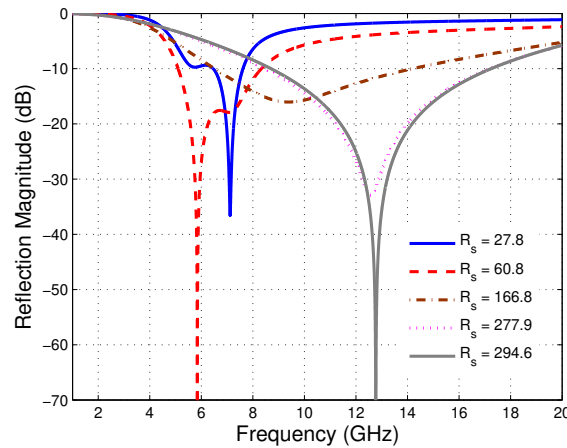
Figure 15. Reflection magnitude of the single-layer mushroom structure for different values of sheet resistivity R_s (in Ω), $\theta = 30^\circ$.

To obtain a range of values for R_s for different incident angles, we plotted the reflection magnitude curves (shown in Fig. 15) for various R_s varying from 0 to ∞ (results for $R_S = 0$ and ∞ are not included here) for a TM-polarized plane wave incident at 30° to the normal. Clearly, one can notice the deviation of the reflection nulls as R_s is increased. Then, we fix the range of R_s where perfect reflection nulls are obtained. Based on this fact, from Fig. 15, the range of R_s is 60.8 - 294.6 Ω. A similar procedure is repeated for $\theta = 60^\circ$ and the range of R_s is found to be 94.03-146.38 Ω. From Fig. 13(b), the range of R_s for 45° can be given as 70.6-241.8 Ω. Then, based on these values of R_s, a unique range that fits for all angles of incidence (up to 60°) can be found: $(94.03 - 146.38)$ Ω for the case under study. A further optimization procedure limited to the above range gives us an optimum value of $R_s = 106.54 \, \Omega$, which is the one used in the absorber design in Fig. 11.

3.2.2. Two-layer mushroom HIS structure with thin resistive patches

The goal of this section is two-fold. The first being the applicability of the derived ABCs (Section 2.2) for the interface of two uniaxial wire media with thin resistive patches at the junction. The second aim is to improve the performance of the single-layer mushroom HIS absorber. To achieve these goals, we first design an absorber over a wide range of frequencies (wider than the single-layer structure) using the homogenization model (discussed in Section 2.3) and compare its results with the full-wave HFSS simulations.

Figure 16 shows the two-layer mushroom HIS absorber, which consists of two wire media embedded in a dielectric host media, loaded with thin resistive patch arrays, and backed by a ground plane. The parameters of the dielectric slabs used in the design together with the dimensions and sheet resistivity values of the square patches are given in the caption of Fig. 16. Figures 17(a) and 17(b) show the reflection magnitude behavior of the two-layer HIS absorber with and without vias for oblique angles of incidence. At first instance, it is clear that the structure with vias offers a significant improvement in the bandwidth, and at the same time shows an enhancement in the absorption level when compared to the reference structure without vias. For example, for $\theta = 60^\circ$, it can be noticed that the 20 dB absorption bandwidth of the structure with vias covering the frequency band from 9.03 GHz to 25.29 GHz has a 55.5% bandwidth increase in comparison to the structure without vias with the
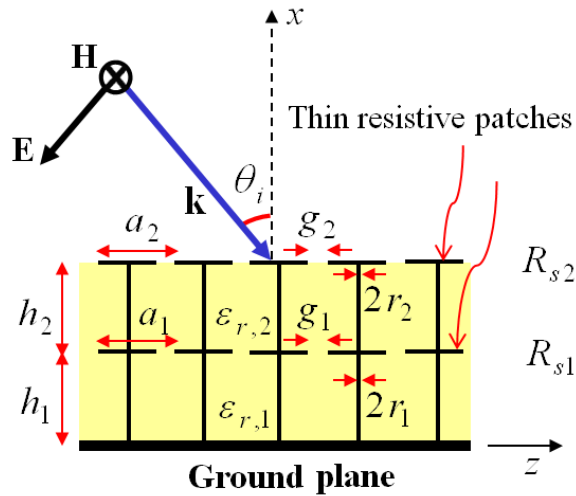
Figure 16. Two-layer mushroom-type HIS absorber with thin resistive patches. Structural parameters used in this work: $h_1 = h_2 = 3.2\,\text{mm}$, $\varepsilon_{r,1} = 2.2$, $\varepsilon_{r,2} = 1.33$, $r_1 = r_2 = 0.05\,\text{mm}$, $a_1 = a_2 = 5\,\text{mm}$, $g_1 = g_2 = 0.1\,\text{mm}$, $R_{s1} = 196\,\Omega$, $R_{s2} = 1078\,\Omega$.

frequency band from 12.67 GHz to 18.86 GHz. Referring to Fig. 17(a), it can be noticed that the results obtained using the nonlocal homogenization model agree very well with the HFSS results in the entire frequency band. This also verifies the new ABCs derived in Section 2.2 for the interface of two uniaxial wire media with thin resistive patch at the junction. This would not be possible using the PEC-ABC (discussed in Section 3.1 for the single-layer mushroom structure with thin metal/graphene patch), which indicates that the new ABCs are in fact important to capture the physics at the thin resistive patch junction of two uniaxial wire media.
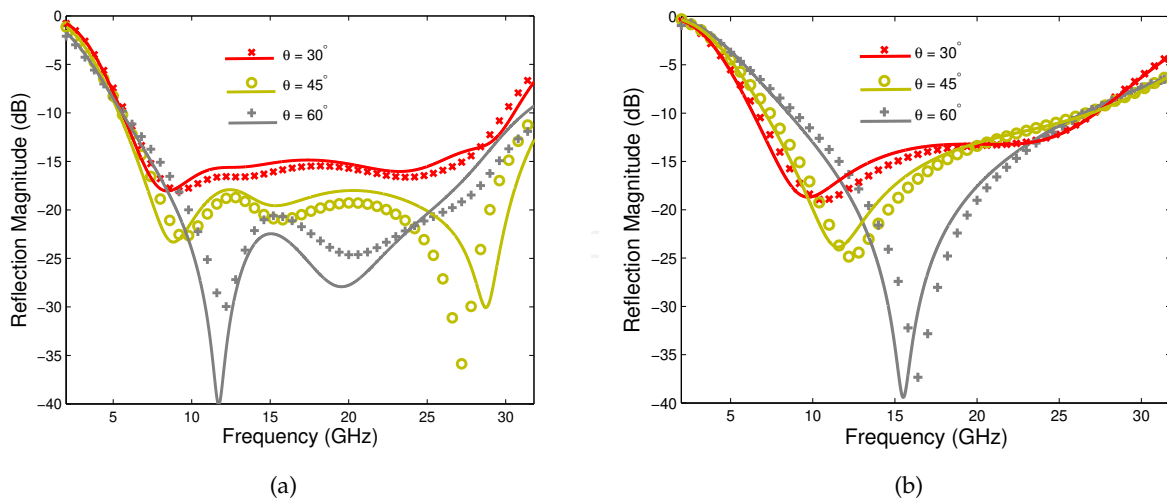

Figure 17. Comparison of analytical (solid lines) and full-wave HFSS results (crosses, circles, and plus signs) of the reflection coefficient for the two-layer HIS absorber excited by a TM-polarized plane wave at oblique angles of incidence θ: (a) with vias. (b) without vias.

Due to increased degrees of freedom in the two-layer structure when compared to the single-layer structure, one can easily see the differences in the relative bandwidth of

absorption of Figs. 17(a) and 17(b), when compared to Figs. 12(a) and 12(b). Even though, the results of the two-layer mushroom structure show significant improvements in the bandwidth and the absorption level, there can be many design solutions (with different R_s) which can yield better results than that shown in Fig. 17(a). Hence, designing an absorber with optimum performance, particularly with many degrees of freedom, is a challenging task. The simpler way is to use the analytical procedure described in the previous section for designing a single-layer mushroom absorber. Although, this procedure may seem simple for the single-layer structure, implementing it for the two-layer structure is a tedious task and, hence, that design procedure is not explained here for the sake of brevity. The other way is to use the numerical optimization techniques [27, 28].
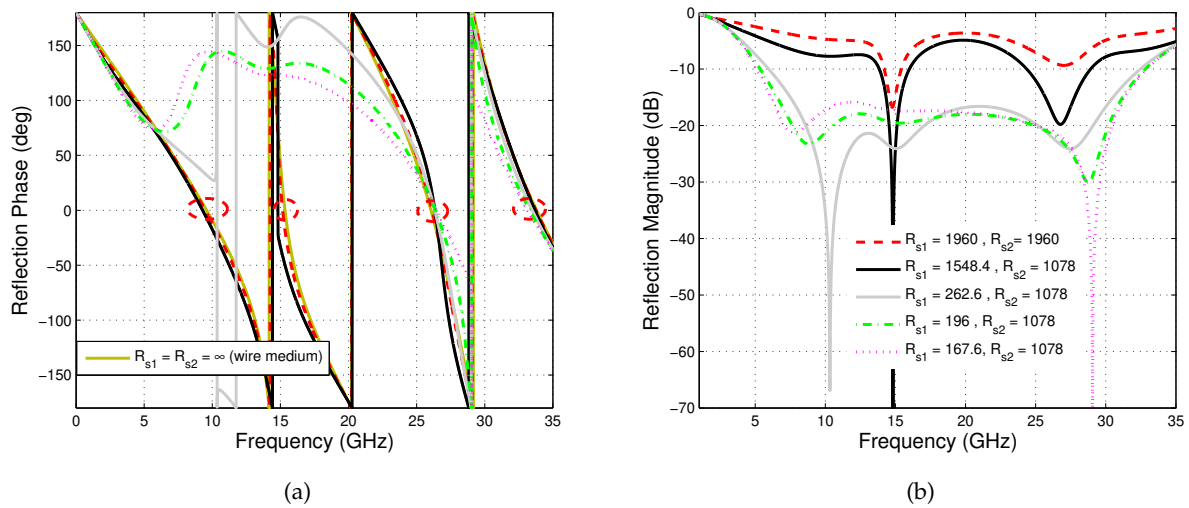

Figure 18. a) Phase and (b) magnitude of the reflection coefficient of the two-layer mushroom structure for different values of sheet resistivity R_s (in Ω), $\theta = 45°$.

In order to understand the nature of the resonances or the wideband behavior of the two-layer mushroom absorber, here we will use the strategy that was implemented to study the wideband behavior of single-layer mushroom absorber, i.e., studying the reflection magnitude behavior for various R_s ranging from 0 to ∞. Since, the value of sheet resistivity for the patch arrays in the top layer is high ($R_s = 1078\ \Omega$) and low in the bottom layer ($R_s = 196\ \Omega$), one can start the analysis either from the PEC case ($R_s = 0$ in both the layers) or the wire-medium case ($R_s = \infty$ in both the layers). Then, either decrease the sheet resistivities in both the layers at the same time (if the wire-medium case is considered) or increase the sheet resistivities in both the layers at the same time (if the PEC case is considered). The other way is start from either the PEC case or the wire-medium case, then fix R_s in one layer while increasing the R_s in the other (if PEC case is chosen) or fix R_s in one layer while decreasing the R_s in the other (if wire-medium case is chosen). Here, we employ the later strategy, because the goal is to explain the wideband behavior of the absorber with $R_{s1} = 196\ \Omega$ and $R_{s2} = 1078\ \Omega$. Figures 18(a) and 18(b) show the reflection phase and magnitude behavior of the two-layer mushroom HIS structure for different values of R_s. With the resistivity of the top patch array being fixed and by gradually decreasing the resistivity of the patch array in the bottom layer it is observed that the phase behavior starts to deviate from the wire-medium slab case (shown in Fig. 18(a)). It is also observed from Fig. 18(b) that the reflection nulls deviate for varying R_s, and for some cases there are perfect reflection

nulls (similar to the behavior observed in a single-layer mushroom structure) corresponding to the zero phases of the perturbed HIS resonances of the wire-medium slab.
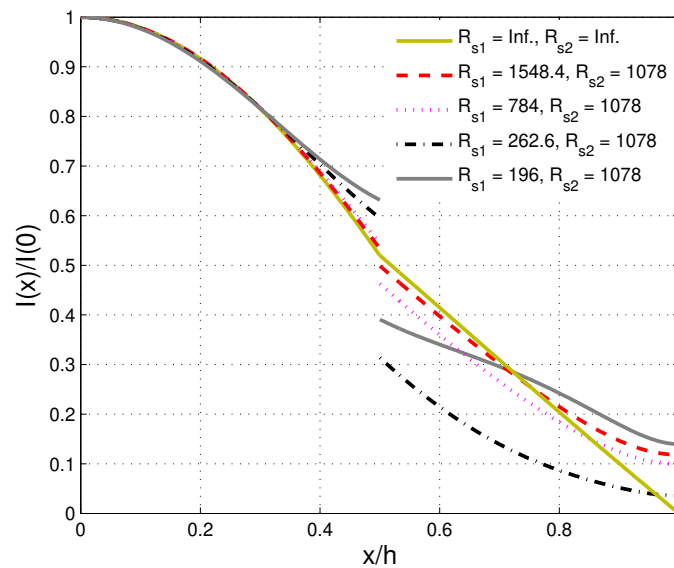

Figure 19. Normalized wire current in the two-layer mushroom structure for different values of sheet resistivity R_s (in Ω) at $f = 15$ GHz, $\theta = 45°$. Here h is the total thickness of the two-layer structure given by $h_1 + h_2$.

This proves the fact that the partial reflection nulls/resonances shown in Fig. 17(a) , for the case of $R_{s1} = 196\,\Omega$ and $R_{s2} = 1078\,\Omega$ are associated with the perturbed HIS resonances of the actual wire-medium slab. It should be noted that the bandwidth enhancement is not only observed for higher angles of incidence, but also observed for smaller angles of incidence. The difference is that for small angles of incidence the electric field interaction with the vias is negligible, and the bandwidth enhancement is due to interactions between the patches in the adjacent layers, and for higher angles of incidence vias play a dominant role in widening the absorption band. Hence, by using the resonances of the mushroom structure, along with the proper choice of dimensions and resistivities of the patch arrays, and with good selection of the permittivities of the dielectric slabs (perforated with metallic vias) the absorption bandwidth can be enlarged, as compared to the case with no vias.

The behavior of current along the vias has also been studied to validate that the resonances are the perturbed HIS resonances of the wire-medium slab. Figure 19 shows the normalized wire current in the two-layer mushroom structure at $f = 15$ GHz. For the values of R_s used in Fig. 18, it can be observed from Fig. 19 that the current along the metallic vias varies significantly, which indicates that the spatial dispersion effects are not suppressed. The reason is that when the R_s is large (conductivity is small), the thin resistive patch resembles a dielectric rather than a metal, and charges accumulate at the tip of the double-sided wire-to-patch junction, which necessitates the ABCs derived in Section 2.2. This behavior is consistent with the results shown in Fig. 10 (Section 3.1) for small values of σ_{2D}, however, it should be noted that the structure analyzed in that section has a single-sided wire-to-patch junction. Since, the current distribution is nonuniform and the phase behavior is close to that of the wire-medium slab case, the resonances of the absorber are indeed the perturbed HIS resonances of the wire-medium slab.
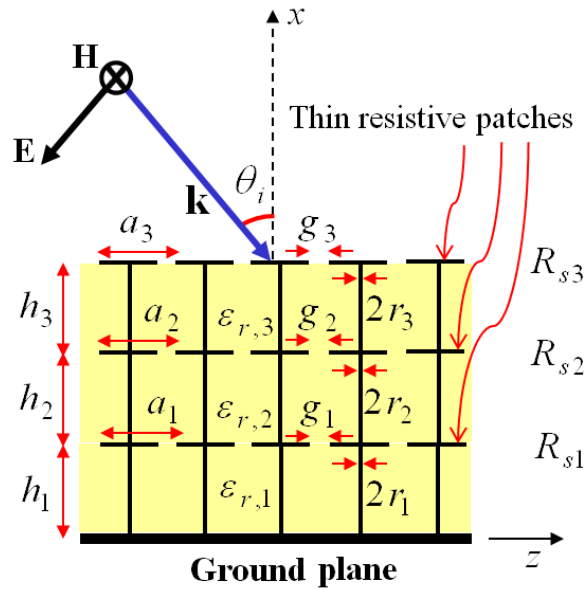
Figure 20. Three-layer mushroom-type HIS absorber with thin resistive patches. Structural parameters used in this work: $h_1 = 2.7\,\text{mm}$, $h_2 = h_3 = 3.2\,\text{mm}$, $\varepsilon_{r,1} = 3.2$, $\varepsilon_{r,2} = 1.8$, $\varepsilon_{r,3} = 1.33$, $r_1 = r_2 = r_3 = 0.05\,\text{mm}$, $a_1 = a_2 = a_3 = 5\,\text{mm}$, $g_1 = g_2 = g_3 = 0.1\,\text{mm}$, $R_{s1} = 196\,\Omega$, $R_{s2} = 588\,\Omega$, $R_{s3} = 1176\,\Omega$.
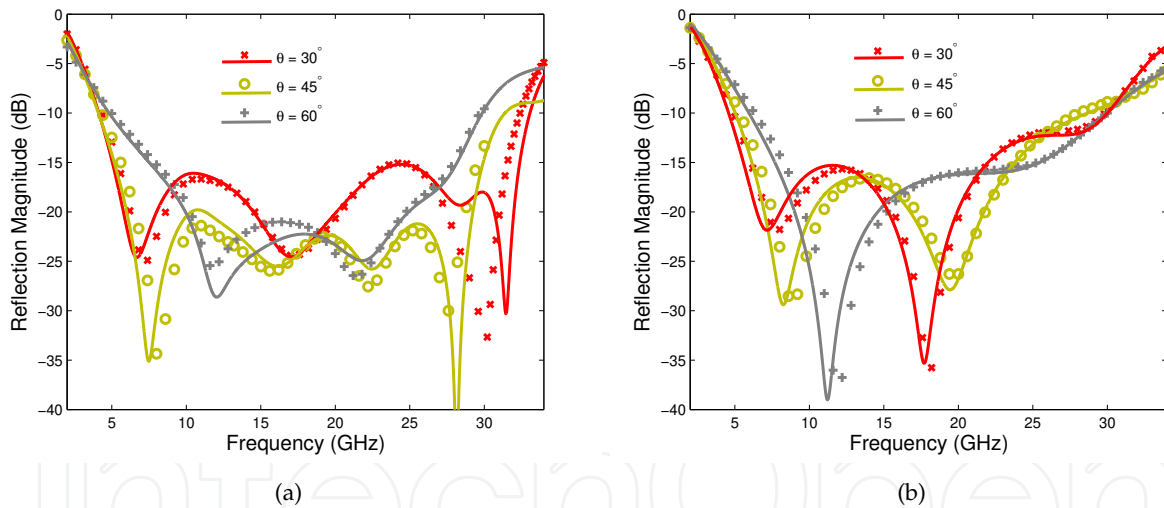

Figure 21. Comparison of analytical (solid lines) and full-wave HFSS results (crosses, circles, and plus signs) of the reflection coefficient for the three-layer HIS absorber excited by a TM-polarized plane wave at oblique angles of incidence θ: (a) with vias. (b) without vias.

3.2.3. Three-layer mushroom HIS structure with thin resistive patches

Figure 20 shows a three-layered mushroom HIS absorber, which consists of three resistive patch arrays separated by dielectric slabs perforated with metallic vias, and backed by a ground plane. The parameters of the dielectric slabs together with the dimensions and sheet resistivities of the square patches are given in the caption of Fig. 20. Figs. 21(a) and 21(b) show the reflection magnitude curves for different incidence angles.

Referring to Fig. 21(a), it can be observed that the analytical results obtained using the nonlocal homogenization model described in Section 2.3 agree very well with the HFSS results. As stated before, the absorption level increases for increasing angles of incidence due to increase in the interaction with vias. By comparing Fig. 21(a) with Fig. 21(b) one can clearly see significant improvements in the absorption bandwidth for the structure with vias for increasing angles of incidence. For example, for $\theta = 60^o$, the 20 dB absorption bandwidth of the structure with vias covering the frequency band from 9.93 GHz to 24.93 GHz shows a 38 % increase in the bandwidth when comparing to the structure with no vias, having the bandwidth from 9.01 GHz to 14.6 GHz. Also, it should be noted that the HFSS results shown in Fig. 21(a) for $\theta = 45^o$ and 60° have been obtained up to $30\,\mathrm{GHz}$ only (due to lack of convergence at higher frequencies).

4. Conclusion

Generalized additional boundary conditions are derived for the interface of two uniaxial wire media with thin resistive sheet at the junction. Based on these conditions a nonlocal homogenization model has been proposed to characterize the reflection properties of the multilayered mushroom HIS structures with thin resistive patches. The homogenization model has been applied to four different structures and the results are validated using the full-wave numerical simulations. An analytical design procedure for selecting resistivities of the patch arrays has been presented. The prospect of using the multilayer mushroom structures as absorbers has been studied. It has been shown that the presence of vias in fact enhances the absorption band and increases the absorption level for increasing angles of incidence for the obliquely incident TM-polarized plane wave.

Author details

Alexander B. Yakovlev[1], Yashwanth R. Padooru[1],
George W. Hanson[2] and Chandra S.R. Kaipa[1]

1 The University of Mississippi, USA
2 University of Wisconsin-Milwaukee, USA

References

[1] J. van Kranendonk & J. E. Sipe. (1977). *Foundtions of the macroscopic electromagnetic theory of dielectric media*, chapter 5 in *Progress in Optics* XV, E. Wolf, (Ed.), New York: North-Holland, 1977.

[2] V. Agranovich & V. Ginzburg. (1966). *Spatial Dispersion in Crystal Optics and the Theory of Excitons*, NewYork: Wiley-Interscience, 1996.

[3] J. D. Jackson. (1998). *Classical Electrodynamics*, Sect. 6.6, NewYork: Wiley, 1998.

[4] D. R. Smith, W. J. Padilla, D. C. Vier, S. C. Nemar-Nasset, & S. Schultz. (2000). A composite medium with simultaneously negative permeability and permittivity, *Phys. Rev. Lett.*, Vol. 84, p. 4184, May 2000.

[5]   L. Landau & E. Lifchitz. (1984). *"Electrodynamics of continuous media," in Course of Theoretical Physics*, 2nd ed., Burlington, MA: Butterworth-Heinemann, 1984, Vol. 8.

[6]   P. A. Belov, Y. Hao, & S. Sudhakaran. (2006). Subwavelength microwave imaging in photonic crystals, *Phys. Rev. B*, Vol. 73, 2006, 033108 (1-4).

[7]   M. G. Silveirinha, P. A. Belov, & C. R. Simovski. (2007). Subwavelength imaging at infrared frequencies using an array of metallic nanorods, *Phys. Rev. B*, Vol. 75, 2007, 035108 (1-12).

[8]   P. A. Belov, R. Marques, S. I. Maslovski, I. S. Nefedov, M. G. Silveirinha, C. R. Simovski, & S. A. Tretyakov. (2003). Strong spatial dispersion in wire media in the very large wavelength limit, *Phys. Rev. B*, Vol. 67, 2003, 113103 (1-4).

[9]   M. G. Silveirinha, C. A. Fernandes, & J. R. Costa. (2008). Electromagnetic characterization of textured surfaces formed by metallic pins, *IEEE Trans. Antennas Propag.*, Vol. 56, No. 2, pp. 405-415, Feb. 2008.

[10] M. G. Silveirinha, C. A. Fernandes, & J. R. Costa. (2008). Additional boundary condition for a wire medium connected to a metallic surface, *New J. Phys.*, Vol. 10, 2008, 053011 (1-17).

[11] M. G. Silveirinha. (2006). Additional boundary condition for the wire medium, *IEEE Trans. Antennas Propag.*, Vol. 54, pp. 1766-1780, 2006.

[12] M. G. Silveirinha. (2009). Broadband negative refraction with a crossed wire mesh, *Phys. Rev. B*, Vol. 79, 2009, 153109 (1-4).

[13] S. I. Maslovski, T. A. Morgado, M. G. Silveirinha, C. S. R. Kaipa, & A. B. Yakovlev. (2010). Generalized additional boundary conditions for wire media, *New J. Phys.*, Vol. 12, 2010, 113047 (1-19).

[14] O. Luukkonen, M. G. Silveirinha, A. B. Yakovlev, C. R. Simovski, I. S. Nefedov, & S. A. Tretyakov. (2009). Effects of spatial dispersion on reflection from mushroom-type artificial impedance surfaces, *IEEE Trans. Microw. Theory Tech.*, Vol. 57, No. 11, pp. 2692-2699, Nov. 2009.

[15] A. B. Yakovlev, M. G. Silveirinha, O. Luukkonen, C. R. Simovski, I. S. Nefedov, & S. A. Tretyakov. (2009). Characterization of surface-wave and leaky-wave propagation on wire-medium slabs and mushroom structures based on local and nonlocal homogenization models, *IEEE Trans. Microw. Theory Tech.*, Vol. 57, No. 11, pp. 2700-2714, Nov. 2009.

[16] A. B. Yakovlev, Y. R. Padooru, G. W. Hanson, A. Mafi, & S. Karbasi. (2011). A generalized additional boundary condition for mushroom-type and bed-of-nails-type wire media, *IEEE Trans. Microw. Theory Tech.*, Vol. 59, No. 3, pp. 527-532, Mar. 2011.

[17] C. S. R. Kaipa, A. B. Yakovlev, & M. G. Silveirinha. (2011). Characterization of negative refraction with multilayered mushroom-type metamaterials at microwaves, *J. Appl. Phys.*, Vol. 109, 2011, 044901 (1-10).

[18] C. S. R. Kaipa, A. B. Yakovlev, S. I. Maslovski, & M. G. Silveirinha. (2011). Indefinite dielectric response and all-angle negative refraction from a structure formed by deeply-subwavelength inclusions, *Phys. Rev. B*, Vol. 84, 2011, 165135 (1-7).

[19] C. S. R. Kaipa, A. B. Yakovlev, S. I. Maslovski, & M. G. Silveirinha. (2011). Mushroom-type high-impedance surface with loaded vias: homogenization model and ultra-thin design, *IEEE Antennas Wireless Propag. Lett.*, Vol. 10, pp. 1503-1506, Dec. 2011.

[20] C. S. R. Kaipa, A. B. Yakovlev, F. Medina, F. Mesa, C. A. M. Butler, & A. P. Hibbins. (2010). Circuit modeling of the transmissivity of stacked two-dimensional metallic meshes, *Opt. Express*, Vol. 18, No. 13, 2010, 13309 (1-12).

[21] D. Sievenpiper, L. Zhang, R. Broas, N. Alexopoulos, & E. Yablonovitch. (1999). High-impedance electromagnetic surfaces with a forbidden frequency band, *IEEE Trans. Microw. Theory Tech.*, Vol. 47, No. 11, pp. 2059-2074, Nov. 1999.

[22] G. W. Hanson. (2008). Dyadic Greens functions and guided surface waves on graphen, *J. Appl. Phys.*, Vol. 103, 2008, 064302 (1-8).

[23] S. Tretyakov. (2003). *Analytical Modeling in Applied Electromagnetics*, Norwood, MA: Artech House, 2003.

[24] O. Luukkonen, C. Simovski, G. Grant, G. Goussetis, D. Lioubtchenko, A. Raisanen, & S. Tretyakov. (2008). Simple and accurate analytical model of planar grids and high-impedance surfaces comprising metal strips and patches, *IEEE Trans. Antennas Propag.*, Vol. 56, No. 6, pp. 1624-1632, Jun. 2008.

[25] Y. R. Padooru, A. B. Yakovlev, C. S. R. Kaipa, F. Medina, & F. Mesa. (2011). Circuit modeling of multi-band high-impedance surface absorbers in the microwave regime, *Phys. Rev. B*, Vol. 84, No. 3, 2011, 035108 (1-11).

[26] Y. R. Padooru, A. B. Yakovlev, C. S. R. Kaipa, G. W. Hanson, F. Medina, F. Mesa, & A. W. Glisson. (2012). New absorbing boundary conditions and homogenization model for multilayered mushroom-type materials: Applications to wideband absorbers, *IEEE Trans. Antennas Propag.*, Vol. 60, No. 12, pp. 5727-5742, Dec. 2012.

[27] L. J. Du Toit & J. H. Cloete. (1996). Electric screen Jauman absorber design algorithms, *IEEE Trans. Microw. Theory Tech.*, Vol. 44, pt. 1, pp. 2238-2245, 1996.

[28] S. Chakravarty, R. Mittra, & N. R. Williams. (2002). Application of the microgenetic algorithm (MGA) to the design of broad-band microwave absorbers using multiple frequency selective surface screens buried in dielectrics, *IEEE Trans. Antennas Propag.*, Vol. 50, pp. 248-296, 2002.

[29] W. J. Lee, J. W. Lee, & C. G. Kim. (2008). Characteristics of an electromagnetic wave absorbing composite structure with a conducting polymer electromagnetic bandgap (EBG) in the X-band, *Composites Science and Technology*, Vol. 68, pp. 2485-2489, 2008.

[30] S. A. Tretyakov, & S. I. Maslovski. (2003). Thin absorbing structures for all incidence angles based on the use of a high-impedance surface, *Microw. Opt. Technol. Lett.*, Vol. 38, pp. 153-157, 2003.

[31] High Frequency Structure Simulator (HFSS) ver. 12.0, Ansoft Corporation, PA, 2010. [Online]. Available: http://ansoft.com